Influence of aortic aneurysm on the local distribution of NO and O2 using image-based computational fluid dynamics

Perinajová, R.; Alvarez-Cuevas, C.B.; Juffermans, J.; Westenberg, J.; Lamb, H.; Kenjeres, S.

Citation

Perinajová, R., Alvarez-Cuevas, C. B., Juffermans, J., Westenberg, J., Lamb, H., & Kenjeres, S. (2023). Influence of aortic aneurysm on the local distribution of NO and O2 using image-based computational fluid dynamics. *Computers In Biology And Medicine*, *160*. doi:10.1016/j.compbiomed.2023.106925

Computers in Biology and Medicine 160 (2023) 106925

Contents lists available at ScienceDirect

Computers in Biology and Medicine

journal homepage: www.elsevier.com/locate/compbiomed

Influence of aortic aneurysm on the local distribution of NO and O_2 using image-based computational fluid dynamics

Romana Perinajová [a,b,*], Concepción Borrás Álvarez-Cuevas [a], Joe Juffermans [c], Jos Westenberg [c], Hildo Lamb [c], Saša Kenjereš [a,b]

[a] Department of Chemical Engineering, Faculty of Applied Sciences, Delft University of Technology, Delft, The Netherlands
[b] J.M. Burgerscentrum Research School for Fluid Mechanics, Delft, The Netherlands
[c] Department of Radiology, Leiden University Medical Center, Leiden, The Netherlands

ARTICLE INFO

Dataset link: https://doi.org/10.5061/dryad.2rbnzs7sq

Keywords:
CFD
Nitric oxide
Oxygen
TAA
4D-flow MRI
Biomarkers

ABSTRACT

There is a pressing need to establish novel biomarkers to predict the progression of thoracic aortic aneurysm (TAA) dilatation. Aside from hemodynamics, the roles of oxygen (O_2) and nitric oxide (NO) in TAA pathogenesis are potentially significant. As such, it is imperative to comprehend the relationship between aneurysm presence and species distribution in both the lumen and aortic wall. Given the limitations of existing imaging methods, we propose the use of patient-specific computational fluid dynamics (CFD) to explore this relationship. We have performed CFD simulations of O_2 and NO mass transfer in the lumen and aortic wall for two cases: a healthy control (HC) and a patient with TAA, both acquired using 4D-flow magnetic resonance imaging (MRI). The mass transfer of O_2 was based on active transport by hemoglobin, while the local variations of the wall shear stress (WSS) drove NO production. Comparing hemodynamic properties, the time-averaged WSS was considerably lower for TAA, while the oscillatory shear index and endothelial cell activation potential were notably elevated. O_2 and NO showed a non-uniform distribution within the lumen and an inverse correlation between the two species. We identified several locations of hypoxic regions for both cases due to lumen-side mass transfer limitations. In the wall, NO varied spatially, with a clear distinction between TAA and HC. In conclusion, the hemodynamics and mass transfer of NO in the aorta exhibit the potential to serve as a diagnostic biomarker for TAA. Furthermore, hypoxia may provide additional insights into the onset of other aortic pathologies.

1. Introduction

Thoracic aortic aneurysm (TAA) is a progressive pathology of the aorta characterized by vessel dilatation, dysfunction of vascular smooth muscle cells, and remodeling of the extracellular matrix, as described by the European Society of Cardiology [1]. Given that this disease is primarily asymptomatic, the rupture of TAA is associated with high mortality rates [2]. Therefore, it is crucial to define new biomarkers to identify the genesis, growth, and rupture of TAA. Recent studies have suggested that the distribution of Oxygen (O_2) and Nitric Oxide (NO) in the aorta could be potential new biomarkers for TAA. TAA tissue exhibits O_2 deficiency (hypoxia) [3]. Moreover, an insufficient supply of O_2 to the aortic wall was linked to the genesis of abdominal aortic aneurysm (AAA) [4,5], likely due to the scarcity of vasa vasorum in this section of the aorta [6]. NO is a regulator in vascular homeostasis and was proposed as a potential key indicator for the development of TAA in patients with Marfan syndrome [7,8]. Elevated NO pathways were observed in individuals with this genetic condition [7], and NO was found to be a significant contributor to the development of TAA in animal models and patients [8]. Therefore, analyzing the behavior of these two molecules in patients with TAA could lead to the identification of direct biochemical markers that estimate the risk of disease progression and rupture.

However, the potential measurement methods for non-invasive assessment of O_2 and NO concentration in the lumen and aortic wall currently do not have a sufficient spatial resolution, as reported in recent studies [9–12]. As a viable alternative, we have previously demonstrated the usefulness of image-based computational fluid dynamics (CFD) in providing insights into blood flow dynamics in the aorta [13,14]. Here, we have to emphasize the subject- and patient-specific nature of simulations, where the geometry and boundary conditions should be based on actual measurements, such as 4D-flow magnetic resonance imaging (4D-flow MRI). By utilizing a patient-specific model

---

[*] Corresponding author at: Department of Chemical Engineering, Faculty of Applied Sciences, Delft University of Technology, Delft, The Netherlands.
E-mail address: R.Perinajova-1@tudelft.nl (R. Perinajová).

https://doi.org/10.1016/j.compbiomed.2023.106925
Received 27 November 2022; Received in revised form 4 April 2023; Accepted 13 April 2023

based on 4D-flow MRI, we can expand the CFD model to account for the mass transfer of these species. However, it is imperative to consider the complex interplay between O_2, NO, and various actors in the vascular system to ensure a physiologically accurate representation of the model.

O_2 is transferred within the cardiovascular system by two distinct mechanisms: diffusion as free species in plasma and binding to hemoglobin, a protein in the erythrocytes. The latter process is the primary mode and contributes to over 98% of total O_2 transport. However, at low shear rates, O_2 is released from the hemoglobin, and free diffusion becomes dominant. This process is particularly pronounced in the capillaries and the proximity of the arterial walls in (the low-shear region) of the great vessels. Therefore, modeling both mechanisms simultaneously is essential [15]. Within the arterial wall, O_2 is supplied by both the lumen and the vasa vasorum and consumed by the tissue. For modeling NO, the focus must be on three primary mechanisms: production, transport, and consumption. First, NO production occurs mainly in the endothelial layer of the arterial wall and is moderated by local wall shear stress (WSS) [16,17] due to the activation of endothelial cells. The second mechanism involves NO transport from the endothelial layer to the smooth muscle cells and into the arterial wall, mainly driven by diffusion. In the opposite direction, NO is transported within the lumen by combined diffusion and convection. Finally, the primary NO sink is its reaction with hemoglobin to form a complex and oxidation to nitrate in the lumen. The reaction with cytoglobin is the major contributor to NO consumption in the arterial wall [16,17].

Numerous investigations have been conducted on modeling the transport processes of O_2 [15,18] and NO [19–23] in idealized or large arteries, such as the aorta. However, the combined effects of hemodynamics and both species were not examined in the aorta. As reported by Allen et al. hypoxia can stimulate the release of NO from red blood cells [24] and, by that, affect vasodilation. Thus, understanding the relationship between the distribution of O_2 and NO can yield valuable insights into the hemodynamic regulation of arterial behavior. Finally, although most studies demonstrated the limitations of O_2 and NO transport in the lumen, the effect on the aortic wall and its remodeling are usually omitted due to the increased complexity of the computational model.

In this study, we put forth the hypothesis that the distribution of O_2 and NO in the aorta is significantly influenced by hemodynamics and the presence of an aneurysm and may serve as an indicator for aneurysm pathogenesis. To investigate this hypothesis, we simulated the interplay between blood flow and mass transfer in the aorta and its wall for two molecules: O_2 and NO. To model the aortic wall, we employed a single-layer approximation with averaged properties to incorporate the effect of intima, media, and adventitia. We developed a model for mass transfer of O_2 within the aorta and aortic wall and its consumption by the wall. In addition, we introduce a model for NO production, which is driven by local hemodynamics and biochemical reactions in the blood and aortic tissue. By using this computational framework, we were able to simulate and comprehend the processes that occur within the aorta and aortic wall in greater detail. We conducted simulations of blood flow with the mass transfer of both studied species in two case-specific geometries: a healthy control (HC) and a patient (P) with a root aneurysm. Finally, based on the analysis of hemodynamics and mass transfer properties of these two cases, we propose potential biomarkers that may indicate TAA pathogenesis.

2. Methods

2.1. Studied cases

The Medical Ethics Committee approved this study protocol of the Leiden University Medical Center (G20.149 for P and P18.034 for HC). Moreover, informed consent was signed by both of the subjects. We have studied two different subjects - a healthy control (HC, Fig. 1a) and a patient with a root aneurysm with D_{max} = 5 cm (P, Fig. 1b) .

Table 1
Parameters of 4D-flow MRI sequence for healthy control and patient; res. denotes resolution.

		Healthy control	Patient
Velocity encoding	[cm/s]	150	160
Reconstructed temporal res.	[ms]	28	38
Echo time	[ms]	2.6	2.7
Repetition time	[ms]	4.5	4.6
Flip angle	[°]	10	10
Acquired isotropic res.	[mm]	2.5	2.7
Field of view	[mm^3]	430 × 70 × 280	350 × 80 × 220
Turbo field echo factor	[–]	2	2
Parallel imaging factor	[–]	2.5 × 1.2	2.5 × 1.2

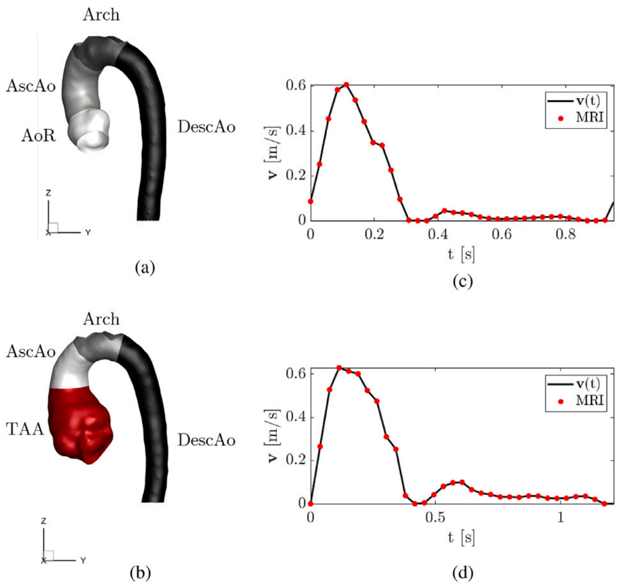

Fig. 1. Pre-processed geometry of healthy control (a) and patient (b) with highlighted regions for analysis (ascending aorta—AscAo, aortic arch—Arch, descending aorta—DescAo, aortic root—AoR (for healthy control only), and thoracic aortic aneurysm—TAA (for the patient only)) and the 4D-flow MRI extracted mean velocity at the inlet with the interpolated velocity **v**(t) for healthy control (c) and patient (d).

2.2. MRI data

Both P (female, 67 years old, heart rate during acquisition: 48 bpm) and HC (male, 80 years old, heart rate during acquisition: 62 bpm) were examined using 4D-flow MRI on a 3T system (Elition, Philips Healthcare, Best, The Netherlands). The MRI acquisition protocol used a hemidiaphragm respiratory navigator with retrospective electrocardiogram gating. All of the additional details about the MRI sequence can be found in Table 1

The subject-specific domain for the lumen-only simulations was obtained by segmenting the 4D-flow MRI data set using CAAS MR Solutions v5.2. (Pie Medical Imaging, Maastricht, The Netherlands). The segmentation protocol is identical for both studied subjects, and the details can be found in our previous study [14]. The segmented geometries, after additional pre-processing using the Vascular Modeling Toolkit (VMTK), can be found in Fig. 1 with highlighted locations of interest—ascending aorta (AscAo), aortic arch (Arch), descending aorta (DescAo), and for P only thoracic aortic aneurysm (TAA).

To create the domain for lumen-wall simulations, the surface of the segmented geometry was offset in the normal direction using Autodesk Meshmixer v3.5 (Autodesk, Inc., California, United States) by the uniform wall thickness T_w = 2.20 mm, based on values typically used in literature [25,26].

2.3. Computational model

2.3.1. Fluid dynamics

The conservation of mass and momentum for the blood flow in the aorta is:

$$\frac{\partial \rho}{\partial t} + \nabla \cdot (\rho \mathbf{v}) = 0 \tag{1}$$

$$\frac{\partial \rho \mathbf{v}}{\partial t} + \nabla \cdot (\rho \mathbf{v} \otimes \mathbf{v}) = -\nabla p + \nabla \cdot (\mu[\nabla \mathbf{v} + (\nabla \mathbf{v})^{\mathrm{T}}]) \tag{2}$$

where $\mathbf{v}$ is the fluid velocity, ρ is the fluid density, μ the fluid dynamic viscosity, and p is the pressure.

2.3.2. Mass transport of O_2

Oxygen transport by plasma (*'passive'* oxygen transport) can be described by the dilute approximation. For this, the convection–diffusion equation for $\mathrm{O_2}$ can be written as:

$$\frac{\partial c^{\mathrm{O_2}}}{\partial t} + \nabla \cdot \left(\mathbf{v} c^{\mathrm{O_2}}\right) = \nabla \cdot \left(\mathscr{D}_f^{\mathrm{O_2}} \nabla c^{\mathrm{O_2}}\right) + r^{\mathrm{O_2}} \tag{3}$$

where $c^{\mathrm{O_2}}$ is the concentration of $\mathrm{O_2}$, $\mathscr{D}_f^{\mathrm{O_2}}$ is the $\mathrm{O_2}$ diffusion coefficient in fluid, and $r^{\mathrm{O_2}}$ is the source/sink which is neglected for the case of passive oxygen transport. For the *'active'* oxygen transport (transport of oxygen bound to hemoglobin) $r^{\mathrm{O_2}}$ reflects the complex reaction process of binding and releasing $\mathrm{O_2}$ from the hemoglobin. For simplification, we assume that the concentration of free $\mathrm{O_2}$ is dependent on the hemoglobin (Hb) saturation as:

$$\mathrm{S} = \frac{\mathrm{pO_2^n}}{\mathrm{pO_2^n} + \mathrm{P_{50}^n}} \tag{4}$$

where S is the saturation of hemoglobin by $\mathrm{O_2}$ (from 0 to 100%), $\mathrm{pO_2}$ is the partial pressure of $\mathrm{O_2}$, n is the Hill's coefficient ($n = 2.7$) and $\mathrm{P_{50}}$ is the partial pressure of $\mathrm{O_2}$ for saturation of 50% ($\mathrm{P_{50}} = 26.6$ mmHg).

Using the $\mathrm{O_2}$ saturation curve and concentration of saturated Hb, and performing a linearization assumption of the $\frac{d\mathrm{S}}{d\mathrm{pO_2}}$ term as shown by Moore and Ethier [15], the mass transfer for $\mathrm{O_2}$ is defined as:

$$\left(1 + \frac{[\mathrm{Hb}]}{\alpha} \frac{n\bar{\mathrm{S}}}{\mathrm{pO_2}} \left(1 - \bar{\mathrm{S}}\right)\right) \left(\frac{\partial \mathrm{pO_2}}{\partial t} + \mathbf{u} \cdot \nabla \mathrm{pO_2}\right) = \nabla \cdot \left[\mathscr{D}_f^{\mathrm{O_2}} \left(1 + \frac{[\mathrm{Hb}]}{\alpha} \frac{\mathscr{D}_c}{\mathscr{D}_f^{\mathrm{O_2}}} \frac{n\bar{\mathrm{S}}}{\mathrm{pO_2}} \left(1 - \bar{S}\right)\right) \nabla \mathrm{pO_2}\right] \tag{5}$$

where α is the solubility coefficient of oxygen, $\mathscr{D}_f^{\mathrm{O_2}}$ is the oxygen diffusion coefficient in blood, $[\mathrm{Hb}]$ is oxygen carrying capacity of hemoglobin in blood, and $\mathscr{D}_c$ is the oxyhemoglobin diffusion coefficient in blood. In this equation, the coefficient on the right-hand side is a non-constant diffusivity of oxygen and the coefficient on the left-hand side as a non-constant carrying capacity of oxygen, respectively. The linearization assumption was shown to be a reasonable simplification of the biological processes as shown by Moore and Ethier for idealized arteries [15] and in our previous study for mass transport of $\mathrm{O_2}$ in the cerebrovascular system [27].

For the $\mathrm{O_2}$ transport in the aortic wall, the convection term is omitted, and we model the process by only considering pure diffusion:

$$\alpha_T \frac{\partial \mathrm{pO_2}}{\partial t} = \alpha_T \nabla \cdot \left(\mathscr{D}_w^{\mathrm{O_2}} \nabla \mathrm{pO_2}\right) - r_w^{\mathrm{O_2}} \tag{6}$$

where α_T is the $\mathrm{O_2}$ solubility in the wall, $\mathscr{D}_w^{\mathrm{O_2}}$ is the $\mathrm{O_2}$ diffusion coefficient in the wall, and $r_w^{\mathrm{O_2}}$ is the volumetric $\mathrm{O_2}$ consumption rate by the wall.

2.3.3. Mass transport of NO

Production of NO occurs in the endothelial layer of the wall and is moderated by local WSS. We have assumed a linear dependency of NO production (r_{NO}) on WSS, defined similarly to Chen et al. [20]:

$$r^{\mathrm{NO}} = r_{ref} \frac{\left|\overrightarrow{\tau_w}\right|}{\tau_{ref}} \tag{7}$$

where r_{ref} is the reference production rate, $\left|\overrightarrow{\tau_w}\right|$ is the WSS magnitude at the wall, and τ_{ref} is the reference wall shear stress. The mass transport of NO in the lumen is modeled using the convection–diffusion equation:

$$\frac{\partial c^{\mathrm{NO}}}{\partial t} + \nabla \cdot \left(\mathrm{v} c^{\mathrm{NO}}\right) = \nabla \cdot \left(\mathscr{D}_f^{\mathrm{NO}}\right) - r_f^{\mathrm{NO}} \tag{8}$$

where c^{NO} is the NO concentration, $\mathscr{D}_f^{\mathrm{NO}}$ is the diffusion coefficient of NO in blood, and r_f^{NO} is the consumption rate of NO by erythrocytes and oxygenation with oxygen, defined as:

$$r_f^{\mathrm{NO}} = k_{\mathrm{O_2}} c_{\mathrm{NO}}^2 + k_{\mathrm{ery}} c_{\mathrm{NO}} \tag{9}$$

where $k_{\mathrm{O_2}}$ is the auto-oxidative NO reaction rate and k_{ery} is the NO reaction rate with erythrocytes. The NO flux from the endothelium to the lumen (J_f^{NO}) was determined using:

$$J_f^{\mathrm{NO}} = A \mathscr{D}_f^{\mathrm{NO}} \left.\frac{dc^{\mathrm{NO}}}{dr}\right|_{r=w} \tag{10}$$

Finally, in the wall, the NO transport is assumed to be diffusion driven:

$$\frac{\partial c^{\mathrm{NO}}}{\partial t} = \nabla \cdot \left(\mathscr{D}_w^{\mathrm{NO}} \nabla c^{\mathrm{NO}}\right) - r_w^{\mathrm{NO}} \tag{11}$$

2.3.4. Boundary conditions and modeling of aortic wall

Fig. 2 visualizes the different domains (lumen (Ω_f) and wall (Ω_w) zones) and boundaries (lumen inlet (Γ_f^{in}), wall inlet (Γ_w^{in}), lumen outlet (Γ_f^{out}), wall outlet (Γ_w^{out}), outside wall (Γ_{ext}), and lumen-wall interface (Γ_{f-w})) for lumen-only (a) and lumen-wall (b) simulations. In addition, Fig. 2 also visualizes the dominant means of $\mathrm{O_2}$ and NO mass transport (either convection or diffusion) within the different zones of the computational domain.

We treated the wall as a homogeneous porous medium with modeled superficial velocity as

$$S_i = -\left(\frac{\mu}{\alpha_w} \mathrm{v_i} + \mathrm{C_{2w}} \frac{1}{2} \rho |\mathbf{v}| \mathrm{v_i}\right) \tag{12}$$

where S_i is the source term for the ith (x, y, or z) momentum equation, α_w is the aortic wall permeability, and C_{2w} is the inertial resistance.

Flow boundary conditions: The inlet boundary condition (Γ_f^{in}) was specified as a plug velocity profile using the time-dependent velocity information at the inlet extracted from the reconstructed 4D-flow MRI. The data points for the average velocity at the inlet ($n_{HC} = 34$, $n_P = 32$) were interpolated in time using linear interpolation, Fig. 1(c) for HC and (d) for P.

The outlet boundaries (Γ_f^{out}) were treated for both cases with the assumption of zero-diffusive flux (for all the flow variables) and a mass balance correction. Specifically for the HC and P, each outlet was assigned a fraction of the flow (w_m), which was defined as

$$w_m = \frac{Q_m}{Q_i} \cdot \frac{1}{\sum_{m=1}^{M} w_m} \tag{13}$$

where Q_m is the flow at the respective outlets and M is the total number of outlets ($M_{HC} = 3$, $M_P = 4$). The fluid-wall interface (Γ_{f-w}), endothelium, was treated as a simplified one-dimensional representation of a thin membrane, with specified pressure drop Δp:

$$\Delta p = -\left(\frac{\mu}{\alpha_{f-w}} \mathbf{v} + \mathrm{C_{2f-w}} \frac{1}{2} \rho \mathbf{v}^2\right) \Delta m \tag{14}$$

where α_{f-w} represents the permeability of endothelium, C_{2f-w} is the pressure jump coefficient, and Δm is the endothelial thickness. The

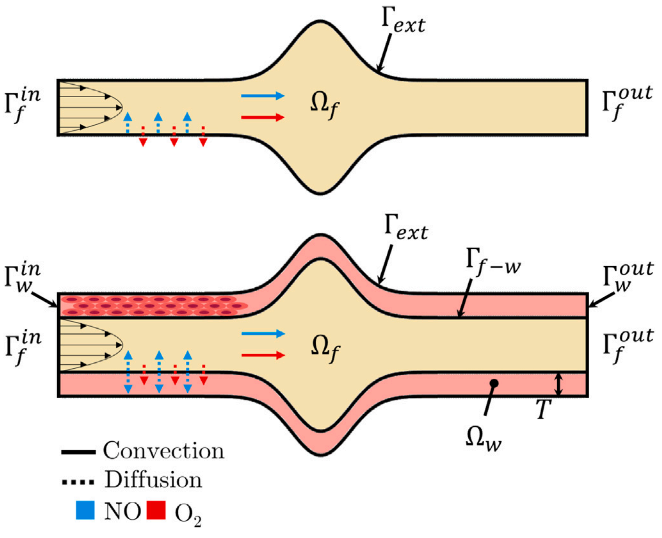

Fig. 2. Visualization of the computational domain with the boundaries for lumen-only (top) and lumen-wall (bottom) simulations with wall thickness T and the main processes of mass transfer for oxygen (O_2) and nitric oxide (NO); the domain includes a lumen (Ω_f) and wall (Ω_w) zones and boundaries: lumen inlet (Γ_f^{in}), wall inlet (Γ_w^{in}), lumen outlet (Γ_f^{out}), wall outlet (Γ_w^{out}), outside wall (Γ_{ext}), and lumen-wall interface (Γ_{f-w}); and highlighted major mechanisms of NO and O_2 mass transfer within the different domains.

Table 2
Physiological parameters of the aortic wall and the weighted averages for the homogeneous wall.

	ϵ [–]	α_w [m^2]	T_w [mm]
Endothelium	5.00e−04	3.20e−21	2.00e−03
Intima	0.983	2.20e−16	0.40
Media	0.258	2.00e−18	1.20
Adventitia	0.85	3.00e−19	0.60
Homogeneous wall	0.551	4.12e−17	2.20
Ref.	[26,28–30]	[26]	[25,26]

Table 3
Biological parameters used in this study.

Parameter	Value	Unit	Ref.
α	2.50e−5	ml O_2/ml blood/mmHg	[15]
α_T	2.40e−5	ml O_2/ml blood/mmHg	[15]
$\mathscr{D}_f^{NO}$	3.30e−9	m^2/s	[21]
$\mathscr{D}_w^{NO}$	8.48e−10	m^2/s	[21]
$\mathscr{D}_w^{O_2}$	0.90e−9	m^2/s	[15]
$\mathscr{D}_f^{O_2}$	1.20e−9	m^2/s	[15]
$\mathscr{D}_c$	1.50e−11	m^2/s	[15]
[Hb]	0.20	ml O_2/ml blood	[15]
$\overline{p_{O_2}}$	75.0	mmHg	[32]
n	2.70	–	[15]
k_{ery}	23.0	s^{-1}	[21]
k_w	0.01	s^{-1}	[21]
k_{O_2}	7.56e−6	nM^{-1} s^{-1}	[21]
r_{ref}	150	μM s^{-1}	[21]
τ_{ref}	2.40	Pa	[21]
$r_w^{O_2}$	2.10e−5	ml O_2/ml tissue/s	[15]

values of the biological parameters for physical properties of the different layers of the aortic wall are listed in Table 2 together with the scaled-averaged properties of the homogeneous (single-layer) walls.

The external wall for lumen-only simulations or vasa vasorum for lumen-wall simulations (Γ_{ext}) was assumed to be identical, with a no-slip condition assumption. Finally, Γ_w^{in} and Γ_w^{out} were assumed to have zero normal velocity.

O_2 and NO mass transfer boundary conditions: The boundary conditions for O_2 and NO at the boundaries shown in Fig. 2 were as follows:

(a) Γ_f^{in}: $p_{O2} = 90$ mmHg; $p_{NO} = 0$ mmHg
(b) Γ_f^{out}: $dp_{O2}/dt = 0$; $dp_{NO}/dt = 0$
(c) Γ_{ext}: $p_{O2} = 45$ mmHg; $dp_{NO}/dt = 0$
(d) Γ_{f-w}: $dp_{O2}/dt = 0$; for NO see Eq. (10)
(e) Γ_w^{in} and Γ_w^{out}: zero normal gradient for O_2 and NO

2.3.5. Physical properties

The shear thinning property of blood was accounted for by applying the Carreau–Yasuda model:

$$\mu(\dot{\gamma}) = \mu_\infty + \left(\mu_0 - \mu_\infty\right) \left[1 + (\lambda\dot{\gamma})^\alpha\right]^{\frac{n-1}{\alpha}} \tag{15}$$

where μ_∞ the viscosity at infinite shear, μ_0 the viscosity at zero shear, λ the relaxation time, $\dot{\gamma}$ the shear rate, α a shape parameter, and n the power-law index. We adopted the exact values for these parameters from Gijsen et al. [31]. The density of the complete mixture was defined using the volume-weighted mixing law:

$$\bar{\rho} = \frac{1}{\sum_i \frac{Y_i}{\rho_i}} \tag{16}$$

where Y_i and ρ_i are the mass fraction and density of species i, respectively. The density for the respective species was defined as: $\rho_{blood} = 1060$ kg/m^3, $\rho_{O_2} = 1.29$ kg/m^3, and $\rho_{NO} = 1.34$ kg/m^3. Since $Y_{blood} \gg \left(Y_{O_2} + Y_{NO}\right)$ the effective density was close to ρ_{blood} with average fluid density $\bar{\rho} = 1057.76$ kg/m^3. The values for all other biological parameters can be found in Table 3.

2.3.6. Mesh and numerical setup

For both of the studied cases concerning lumen-only simulations, we have created a polyhedral mesh with refinement consisting of ten layers close to the wall (Γ_{ext}). The mesh dependency was performed for one of the cases (HC) at the peak-systolic conditions, Appendix. The final meshes consisted of approximately 2.3 mil. cells for HC and 2.2 mil. cells for P.

The mesh consisted of polyhedral elements for the lumen-wall simulations, with refinement close to Γ_{f-w} and Γ_{ext}. The dependency of the solution on the mesh was tested with varying numbers of refinement layers close to the fluid-wall interface, Appendix. The final meshes for lumen-wall simulations consisted of 6.2 mil. cells for HC and 6.5 mil. cells for P.

The simulations were performed using Ansys Fluent 2019 R3 (Ansys, Canonsburg, Pennsylvania, US). The solver setup for this study was as follows: (1) pressure-based solver; (2) PISO for pressure-velocity coupling; (3) second-order upwind discretization for all quantities; (4) implicit time discretization; (5) residuals lower than 1×10^{-5}.

2.3.7. Post-processing and data analysis

MRI-based WSS was estimated using CAAS MR Solutions v5.2, similarly as described in our previous publication [14]. To analyze the hemodynamics and mass transfer of species, we have calculated several (time-averaged) quantities. From the hemodynamical properties, first, the time-averaged wall shear stress (TAWSS) was calculated using the following:

$$\text{TAWSS} = \frac{1}{T} \int_0^T \left|\overrightarrow{\tau_w}\right| dt \tag{17}$$

where T is the cycle length. The oscillatory shear index (OSI) was calculated as follows:

$$\text{OSI} = \frac{1}{2} \left(\frac{\left|\int_0^T \overrightarrow{\tau_w}\, dt\right|}{\int_0^T \left|\overrightarrow{\tau_w}\right| dt} \right) \tag{18}$$

Table 4
The maximal, mean, and standard deviation (σ) of wall shear stress (WSS) for healthy control and patient based on MRI and CFD.

	WSS_{max} [Pa]	WSS_{mean} [Pa]	σ [Pa]
Healthy control			
MRI	4.36	1.35	0.62
CFD	65.16	3.31	2.78
Patient			
MRI	3.29	1.15	0.51
CFD	69.57	6.32	5.39

Finally, the endothelial cell activation potential (ECAP) was calculated as:

$$\mathrm{ECAP} = \frac{\mathrm{OSI}}{\mathrm{TAWSS}} \tag{19}$$

To study the mass transfer of O_2 and NO close to the wall, we have calculated the Sherwood number for species i (Sh_i) as

$$\mathrm{Sh}_i = \frac{-\left(\frac{\partial c_i}{\partial n}\right)_w}{c_{ib} - c_{iw}} \tag{20}$$

where c_i is the local concentration of species i, c_{ib} is the bulk concentration of the species, and c_{iw} is the concentration at the wall. The time-averaged Sh_i can be written as

$$\mathrm{TASh}_i = \frac{1}{T}\int_0^T Sh_i \, dt \tag{21}$$

To estimate the hypoxic area for lumen-only simulations, the species' consumption rate within the wall must be determined. For this, the rate of species consumption can be estimated using non-dimensional Damköhler number (Da), defined as:

$$\mathrm{Da} = \frac{\dot{Q}_{O_2 b} T_w a}{K \mathscr{D}_{O_2} p_{O_2 b}} \tag{22}$$

where $\dot{Q}_{O_2 b}$ is the oxygen consumption rate of arterial tissue, T_w is the arterial wall thickness, a is the mean arterial diameter, K is Henry's constant, $\mathscr{D}_{O_2}$ is the oxygen diffusion coefficient and $p_{O_2 b}$ is the bulk partial pressure of oxygen. The region that suffers from hypoxia due to mass transfer limitations is characterized by the O_2 transport being lower than its consumption by the wall, or $\mathrm{Sh}_{O_2} < \mathrm{Da}$.

Finally, we have defined a few specific parts of the aorta used for further analysis, as shown in Fig. 1. The specific regions are: ascending aorta (AscAo), aortic arch (Arch), and descending aorta (DescAo) (for both subjects). In addition, aortic root (AoR) was defined for analysis of HC and thoracic aortic aorta (TAA) for P.

3. Results

3.1. Validation of hemodynamics in lumen

Fig. 3 shows the comparison of MRI normalized WSS (WSS/WSS_{ave}) to the CFD simulated results. WSS was normalized using the respective average values of WSS for MRI and CFD. The data are visualized at peak systole for both HC (Fig. 3(a)) and P (Fig. 3(b)).

The maximal and average values and standard deviation (σ) of WSS for each of the cases and methods can be seen in Table 4

3.2. Time-averaged hemodynamics in lumen

The time-averaged quantities that quantify the hemodynamics close to the aortic wall are shown in Fig. 4 for both HC and P. We have visualized the time-averaged wall shear stress (TAWSS [Pa]), Oscillatory Shear Index (OSI [−]), and the Endothelial Cell Activation Potential (ECAP [Pa^{-1}]). For both HC and P, the color bar limits are set to the same values to allow an adequate comparison.

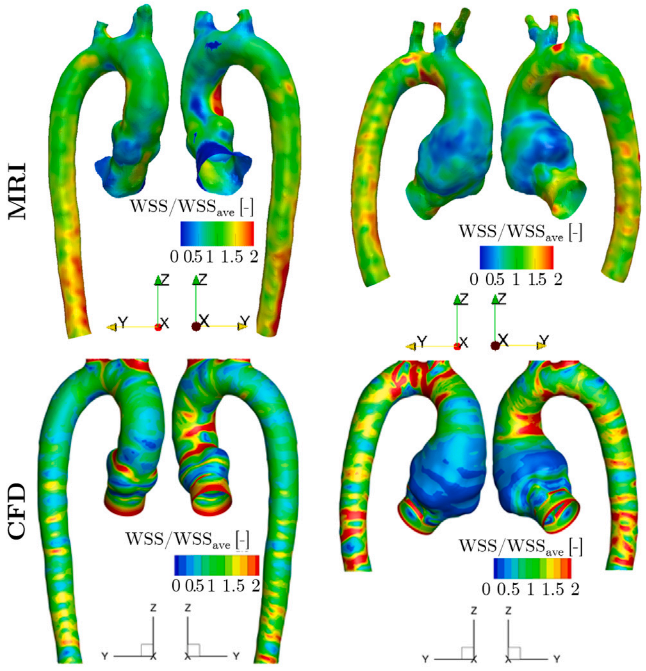

(a) Healthy Control
(b) Patient

Fig. 3. Comparison between MRI (top) and CFD (bottom) at peak systole for the healthy control (HC - (a)) and patient (P - (b)) in terms of normalized wall shear stress (WSS/WSS_{ave} [−]) where WSS was normalized by the respective spatially average values (WSS_{ave}) for MRI and CFD.

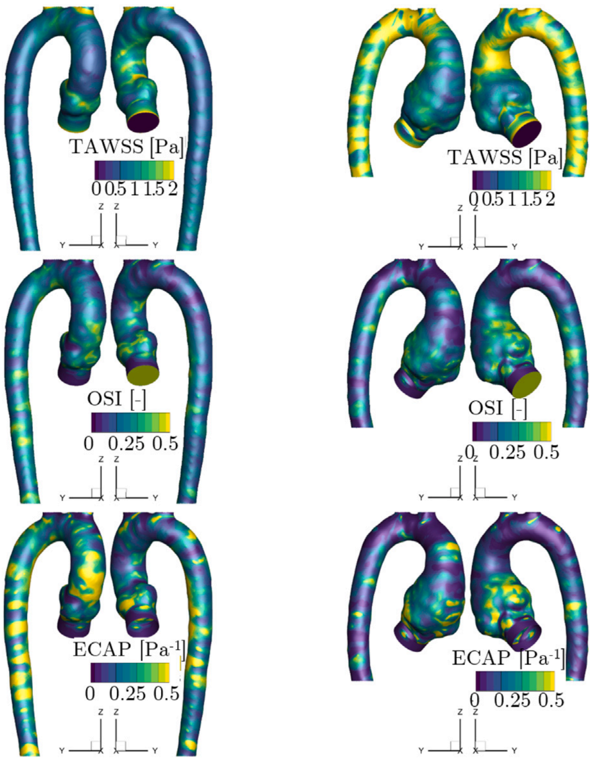

(a) Healthy Control
(b) Patient

Fig. 4. Time-averaged wall shear stress (TAWSS [Pa]), Oscillatory Shear Index (OSI [−]), and Endothelial Cell Activation Potential (ECAP [Pa^{-1}]) for healthy control (a) and patient (b) in the lumen-only approximation of aorta.

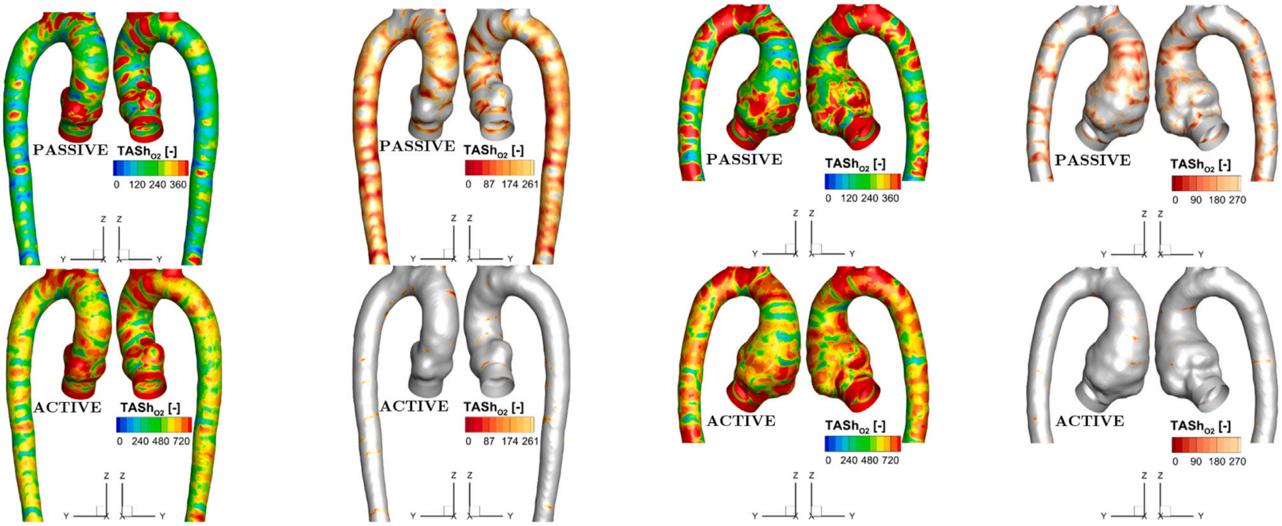

(a) (b) (c) (d)

Fig. 5. Time-averaged Sherwood number for (from top to bottom) oxygen ($TASh_{O_2}$ [−]) for passive oxygen transport (top) and active oxygen transport (bottom) and Time-averaged Sherwood number for nitric oxide transport ($TASh_{NO}$ [−]) for healthy control (a) and patient (c) and the estimation of hypoxic areas based on Sherwood number lower then Damköhler number (Da<Sh) visualized using $TASh_{O_2}$ [−] for healthy control (b) with $Da_{HC} = 290$ and patient (d) with $Da_P = 304$ in the lumen-only approximation of aorta.

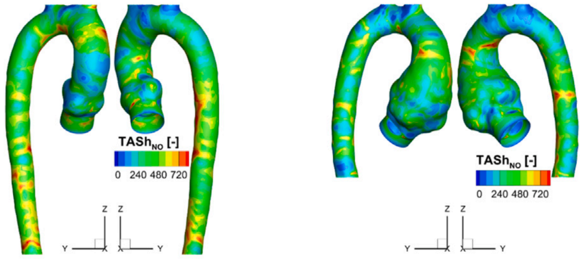

(a) (b)

Fig. 6. Time-averaged Sherwood number for nitric oxide transport ($TASh_{NO}$ [−]) for healthy control (a) and patient (b) in the lumen-only approximation of aorta.

Table 5
Average values of hemodynamic mass transfer properties for healthy control (HC) and patient (P) within specific sections of aorta (ascending aorta—AscAo, aortic arch—Arch, descending aorta—DescAo, for H only aortic root—AoR, and for P only aneurysm—TAA); the evaluated variables are: relative percentage hypoxic area for passive (A_{hypP}) and active (A_{hypP}) transport, time-averaged wall shear stress (TAWSS), oscillatory shear index (OSI), endothelial cell activity potential (ECAP), time-averaged Sherwood number for passive oxygen transport ($TASh_{O2P}$), active oxygen transport ($TASh_{O2A}$), and nitric oxide transport ($TASh_{NO}$).

		Healthy control			Patient			
		AscAo	Arch	DescAo	TAA	AscAo	Arch	DescAo
Hemodynamics								
TAWSS	[Pa]	0.95	0.90	0.65	1.06	1.49	2.06	1.63
OSI	[-]	0.21	0.16	0.21	0.23	0.13	0.09	0.17
ECAP	[Pa^{-1}]	0.37	0.18	0.34	0.25	0.29	0.06	0.13
Mass transfer								
$TASh_{O2P}$	[−]	286	316	179	322	260	416	298
$TASh_{O2A}$	[−]	643	686	559	671	623	745	660
$TASh_{NO}$	[−]	311	280	432	301	351	199	338
Hypoxic area								
A_{hypP}	[%]	50	43	88	38	58	19	47
A_{hypA}	[%]	2.2	2.6	3.9	1.3	3.5	0.8	1.6

3.3. Mass transfer of O_2 and NO in lumen

To study the effects of O_2 and NO mass transfer in the lumen, we have calculated and visualized the time-average Sherwood number (TASh [−]) for the different species in Fig. 5. For O_2, $TASh_{O_2}$ is shown for two different modes of transport are shown—passive (top) and active (bottom). The data range for the passive $TASh_{O_2}$ is half of active $TASh_{O_2}$.

Fig. 5(b) and (d) also show the estimated hypoxic regions for passive and active O_2 mass transport. The locations of hypoxia occur if the O_2 mass transfer towards the wall (Sh) is lower than its consumption by the wall (Da), i.e., if $TASh < Da$ applies. We have estimated Da (as defined in Eq. (22)), separately for HC and P based on the average diameter of the aorta (healthy portion only for P). The estimated values were: $Da_{HC} = 290$ for HC and $Da_P = 304$ for P. Additionally, we have calculated the relative percentage area affected by hypoxia (A_{hyp}), defined as the hypoxic area per the total area, in the ascending aorta (AscAo), aortic arch (Arch) and descending aorta (DescAo). A_{hyp} for both studied subjects is shown in Table 5 (for passive and active O_2 transport).

Finally, Fig. 6(b) shows the time-averaged Sh for NO ($TASh_{NO}$ [−]) for both studied cases.

Next, we have visualized the circumferential average of various hemodynamic quantities (TAWSS, OSI, and ECAP) together with TASh for NO and O_2 (passive and active) alongside the normalized centerline length (l/l_{max}) for both studied subjects, Fig. 7. The centerline length was normalized by its maximum (l_{max}), and the different sections of the aorta are highlighted (ascending aorta—AscAo, aortic arch—Arch, descending aorta—DescAo, and for P only: aneurysm—TAA). For HC, to achieve an adequate comparison, only the data within the range of centerline length for P were taken into account since the simulated domain was longer. The average values in the regions of interest (Aor, AscAo, Arch, DescAo, and TAA for P) of all the studied quantities for HC and P are shown in Table 5.

Until now, we have primarily focused on the absolute behavior of the cardiac cycle by analyzing the time-averaged quantities. While this approach allows for understanding the complete mass transfer and blood flow behavior, it may cause the concealment of specific details due to the averaging. Therefore, we have extracted data at peak systole alongside two lines (inseam and outseam) for both studied subjects, as shown in Fig. 8. We have visualized WSS with Sh for NO and active O_2 mass transport. The length of the inseam and outseam (l) were non-denationalized using the respective maximal values. Finally, the boundaries for the specific regions of interest are highlighted.

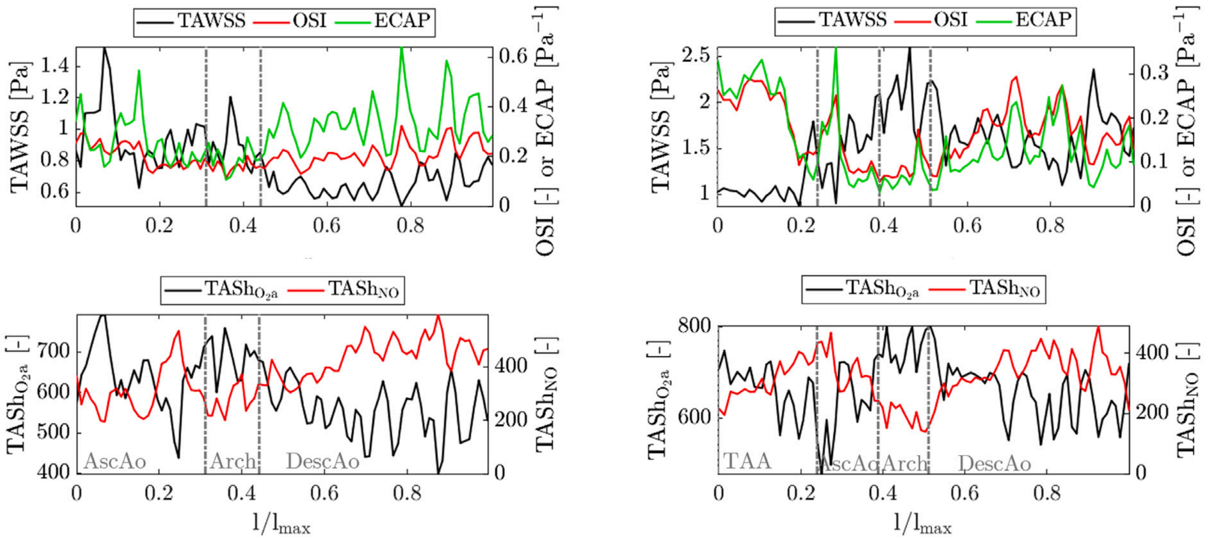

(a) Healthy Control

(b) Patient

Fig. 7. Circumferential average alongside the normalized centerline length (l/l_{max}) for: time-averaged wall shear stress (TAWSS [Pa]), oscillatory shear index (OSI [−]), endothelial cell activation potential (ECAP [Pa^{-1}], Time-averaged Sherwood number for active oxygen (TASh$_{O_2a}$ [−]), and Time-averaged Sherwood number for nitric oxide (TASh$_{NO}$ [−]); for healthy control (a) and patient (b) in the lumen-only approximation of aorta; we divided the domain to highlight the ascending aorta (AscAo), aortic arch (Arch), descending aorta (DescAo), and aneurysm (TAA—for the patient only).

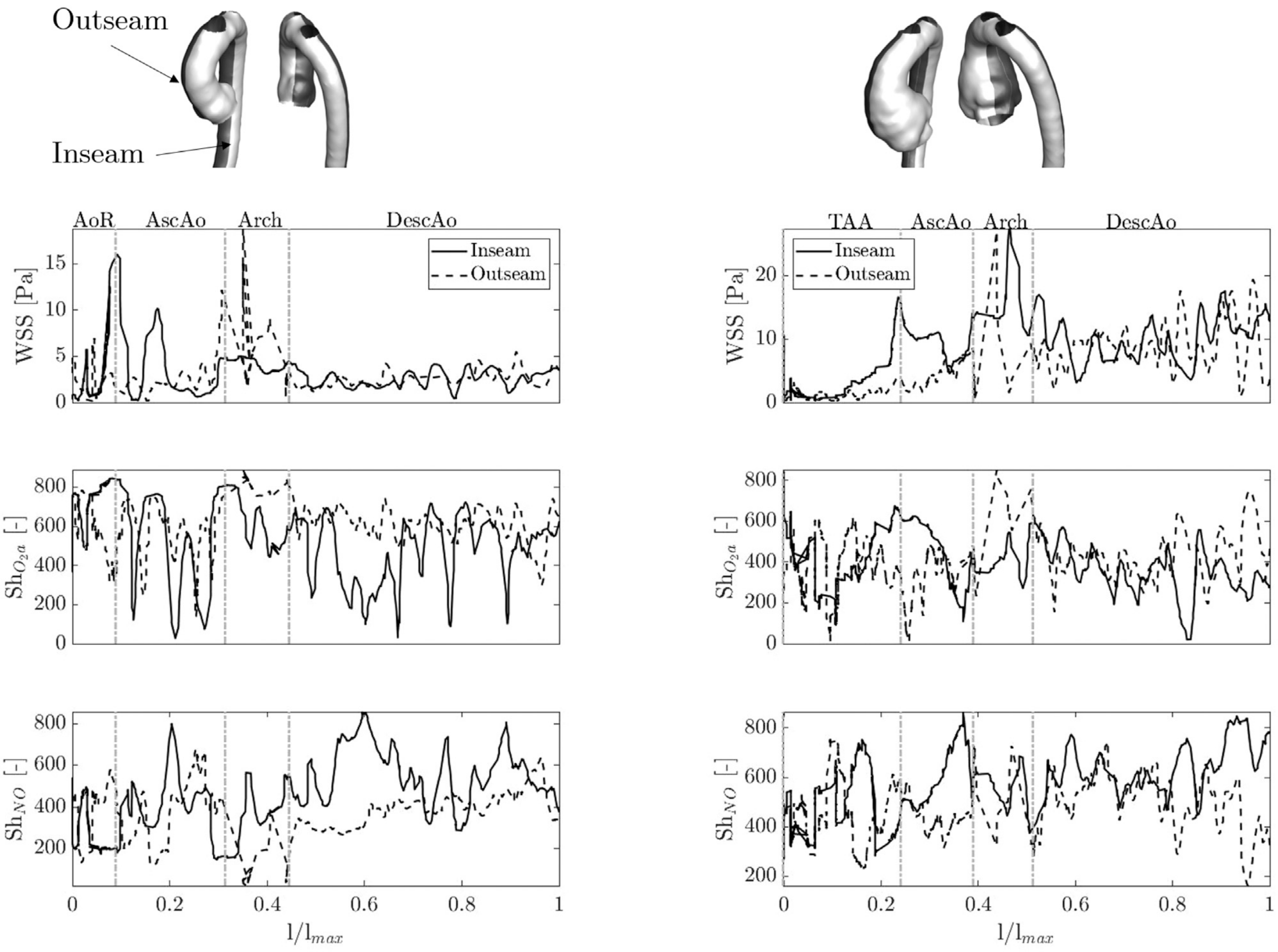

(a) Healthy Control

(b) Patient

Fig. 8. Wall shear stress (WSS [Pa]), Sherwood number for active oxygen (Sh$_{O_2a}$ [−]), and Sherwood number for nitric oxide (Sh$_{NO}$ [−]) alongside the normalized centerline length (l/l_{max}) extracted alongside the inseam and outseam for: healthy control (a) and patient (b) in the lumen-only approximation of aorta; the domain is divided to highlight the ascending aorta (AscAo), aortic arch (Arch), descending aorta (DescAo), and aneurysm (TAA—for the patient only).

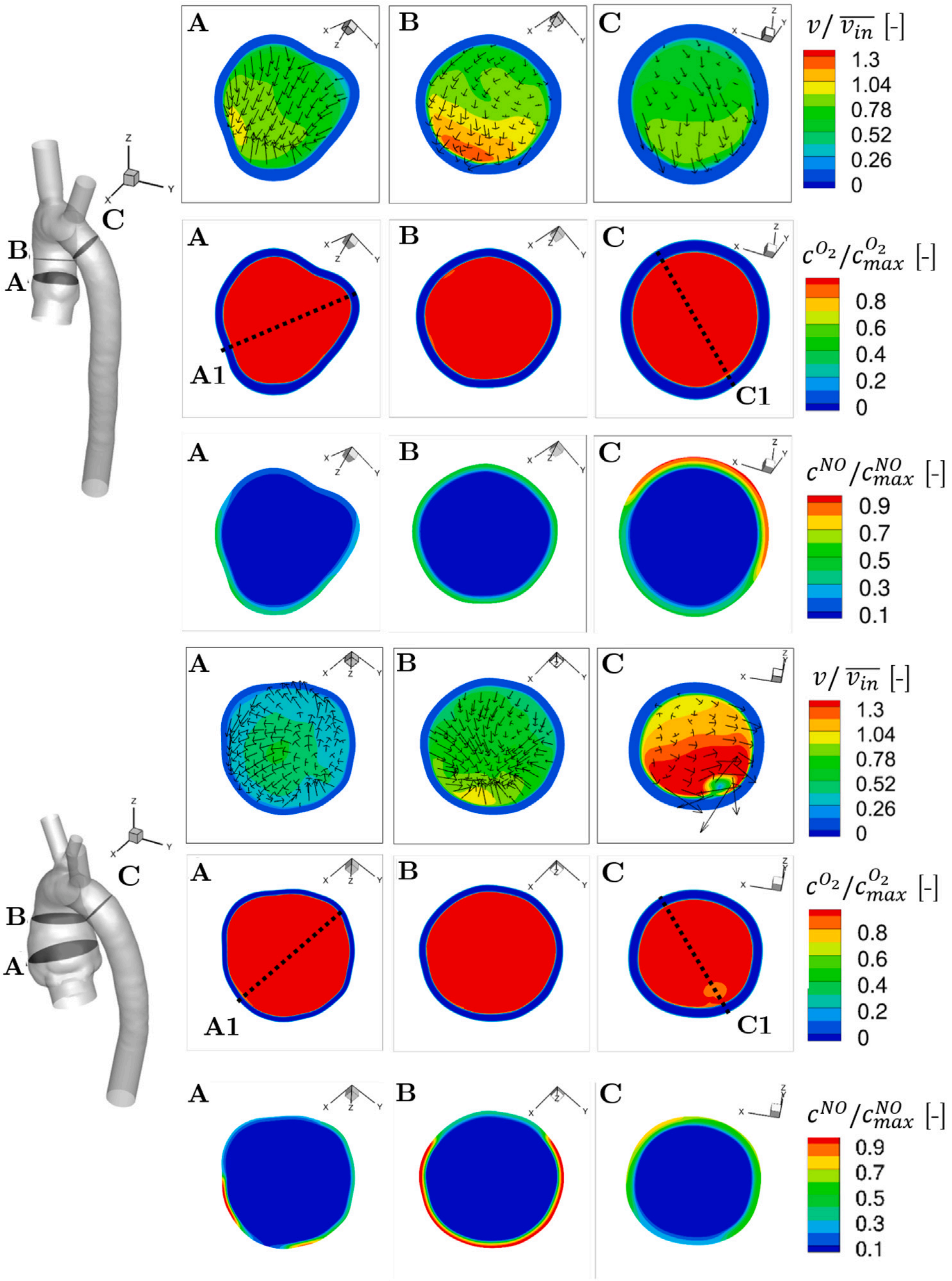

Fig. 9. Normalized concentration of O_2 ($c^{O_2}/c^{O_2}_{max}$ [−]) and NO (c^{NO}/c^{NO}_{max}) [−]) and normalized velocity magnitude ($v/\overline{v_{in}}$ [−]) for healthy control (top) and patient (bottom) visualized at several locations of interest.

3.4. *Mass transfer of O_2 and NO in aortic wall*

Fig. 9 shows the normalized concentration of O_2 ($c^{O_2}/c^{O_2}_{max}$ [−]) and NO (c^{NO}/c^{NO}_{max} [−]) visualized at different locations of interest (A - root, B - ascending aorta, C - after arch) alongside with the velocity field with normalized velocity magnitude ($v/\overline{v_{in}}$ [−]) for peak systole. The concentration of both species was normalized using the inlet (maximal) $c^{O_2}_{max}$ for O_2 and global maximum c^{NO}_{max} for NO. The velocity magnitude was normalized using the average velocity at the inlet $\overline{v_{in}}$. Additionally, the data are visualized alongside the lines extracted from (A1 and C1) in Fig. 10. We visualized the data alongside a normalized diameter of the particular slice (d/d_{max}), with d_{max} being the maximal lumen diameter of the slice.

4. Discussion

In this study, we have conducted simulations of blood flow and combined mass transfer of O_2 and NO in a subject-specific aorta and its wall, focusing on two cases: a healthy control (HC) and a patient (P) with a root aneurysm. The simulations were based on 4D-flow MRI measurements, from which geometry and boundary flow conditions were extracted. To examine flow dynamics in the wall, we have developed a simplified, single-layer model of the aortic wall, featuring a constant thickness and physical properties based on the average of intima, media, and adventitia.

Since the information for the blood flow was derived from a single 4D-flow MRI measurement, we used this data to validate our simulated flow field within the lumen. Comparing normalized values of WSS for

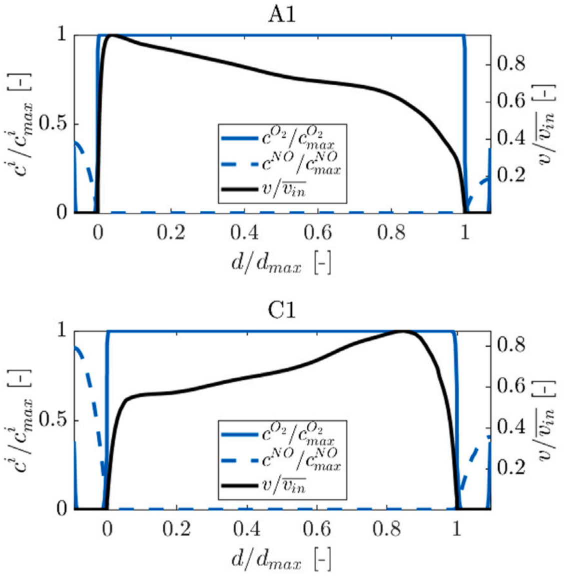

(a) Healthy Control

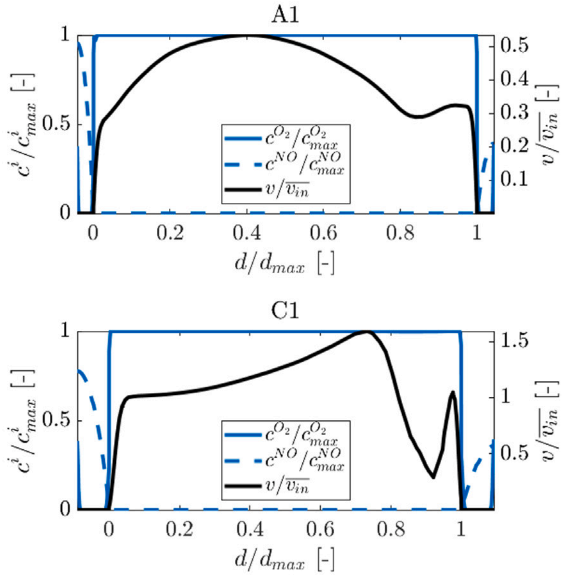

(b) Patient

Fig. 10. Normalized concentration of O_2 and NO (c^i/c^i_{max} [−]) and normalized velocity magnitude ($v/\overline{v_{in}}$ [−]) for healthy control (top) and patient (bottom) visualized alongside extracted line with normalized distance for the particular location (d/d_{max}), where $d_m ax$ is the maximal lumen diameter.

both cases at peak systole, the simulated blood flow shows similar behavior to the measured one. We note that while there are some differences between the two methods, as reported in our previous studies [13,14,27], the data from both methods agree well in capturing the global behavior of WSS including areas of local maximal and minimal values. We conclude that the blood flow data obtained from simulations adequately represent reality, as demonstrated in our earlier research [13,14].

Besides WSS within the aorta, several previous studies have focused on time-averaged hemodynamical quantities to establish potential biomarkers for the progression of TAA. In this study, we have explored potential biomarkers for the progression of TAA by examining the effects of time-averaged hemodynamical quantities such as TAWSS, OSI, and ECAP, as shown in Fig. 4, in both HC and P cases. When comparing the healthy and aneurysmal cases, the section suffering from TAA indicates few striking characteristics. For instance, TAWSS shows a global minimum in the area of TAA, similar to previously reported behavior in TAA and AAA [33,34]. Moreover, TAA also suffers from higher OSI than the healthy aorta, and the ECAP is significantly higher in the location of TAA compared to the rest of the aorta. These three characteristics indicate a potentially higher risk for additional growth or rupture due to impaired endothelial cell activity. Endothelial cells respond to non-physiological values of WSS and change in the direction of WSS during the cardiac cycle in various ways [35,36], which, among others, affects the production of different species (like NO). However, since we have only simulated two subjects, we cannot conclude whether TAWSS, OSI, and ECAP are reliable predictors of aneurysms. Instead, we suggest that these hemodynamical indicators should be further investigated in a large population study with multiple HC and patients with TAA, as we observed apparent differences between HC and P in these variables. Moreover, to determine if these biomarkers are associated with aneurysm growth, longitudinal data are necessary to be included in the analysis.

We also highlight the region of the AscAo immediately following the TAA. In this region, the artery experiences a sudden increase in TAWSS (in the transition between TAA and the *'healthy'* part), as can be observed in Fig. 7. This behavior is also evident in the instantaneous WSS at peak systole, as depicted in Fig. 8. Additionally, a sudden increase in OSI and ECAP occurs further downstream of the TAA, as shown in Fig. 7. In contrast, such behavior is not evident in the AscAo of HC. These findings suggest that a further aberrant blood flow occurs downstream of TAA, potentially leading to additional growth, the genesis of the secondary aneurysm, or even the onset of aortic dissection (AD). Consistent with this observation, Peng et al. have demonstrated a strong correlation between the hemodynamics close to the tear in AD and aberrant blood flow, as well as high OSI [37]. Furthermore, TAA is considered a risk factor for AD [1].

In addition to hemodynamics, we also simulated the mass transfer of O_2 and NO in the lumen and aortic wall. Within the lumen, both species show non-uniform distribution. Moreover, we found an inverse correlation between the two species, as regions with lower O_2 exhibited higher NO concentration and vice-versa, as depicted in Fig. 7 for the time-averaged quantities and in Fig. 8 for instantaneous mass transfer at peak systole. We can also observe similar behavior regarding concentration boundary layer thickness within the lumen. For both cases, the boundary layer is very thin, with a sudden decrease in concentration for both species. The observed relationship can be explained by the relative thickness of the concentration boundary layer compared to the momentum boundary layer, expressed in Schmidt number (Sc). For both species, Sc is very high, with values of $\mathrm{Sc}^{NO} \sim 1000$ for NO and $\mathrm{Sc}_p^{O_2} \sim 3000$ and $\mathrm{Sc}_a^{O_2} \sim 30000$ for passive and active O_2 respectively. Thus, NO is almost instantly consumed within the lumen, and the O_2 concentration gradient at the wall is very steep, with minimal influence from lumen-side mass transfer limitations. Similar observations were previously reported for idealized arteries by Plata et al. for NO [19] and Moore and Ethier for O_2 [15], as well as for mass transfer in aorta [21].

In regard to O_2 mass transfer, this phenomenon is also manifested in the estimation of hypoxic regions within the aorta. The hypoxic area can be estimated by comparing the mass transfer towards the wall (Sh) with the estimated consumption of the wall (Da). In our study, the hypoxic region occurred if Sh was lower than Da = 290 for HC and Da = 304 for P. Notably, the estimated hypoxic area for passive O_2 is much greater than for the active O_2. For the latter mentioned, just one to four percent of the total aortic area suffers from estimated hypoxia. In addition, we can observe subtle differences between HC and P. The hypoxic area is lower in P, particularly in DescAo, which could also be attributed to the estimated value of Da. Moreover, Da was estimated to be lower in HC. This discrepancy in Da was influenced by the calculated average diameter (a) of the artery, which was higher for P, even though we excluded the majority of TAA from the calculations. To address this limitation, an adaptive calculation of Da should be employed, with variable *a* as a function of centerline distance. However, when considering only estimated hypoxia in P, no significant differences between the healthy tissue and TAA are apparent.

Nevertheless, the impact of hemodynamics on O_2 concentration persists. In the case of P, a distinct recirculation zone is evident just after the arch (slice C in Fig. 9). This recirculation zone causes a slight reduction in O_2 concentration. Similar hemodynamics-induced variations in concentration were previously observed in the stenotic region of the carotid artery [18]. Thus, monitoring areas with aberrant blood flow within the aorta is crucial, as prolonged hypoxia can trigger extracellular matrix remodeling and degradation [38] and play an essential factor in aneurysm pathogenesis [39].

The distribution of NO closely follows the TAWSS distribution in the aorta since WSS triggers NO production. Consequently, NO is unevenly distributed in the lumen and the aortic wall, as can be observed in our simulations as well as previously reported NO distribution in the aortic wall [21] and in coronary arteries [23]. Notably, the distribution of NO within the aortic wall differs significantly between P and HC, particularly near the root, as shown in Figs. 9 and 10, due to the presence of TAA Here, the gradient in NO concentration is very high between the inner and outer curves of the aorta, with additional disruptions in the proximity of the inner curve. These variations could indicate dysfunction of the arterial wall due to uneven stimulation of smooth muscle cells within TAA, which may contribute to further growth.

We identified several limitations in our study. Firstly, we restricted our analysis to only two subjects, precluding us from drawing a statistically significant conclusion regarding the effects of limitations in O_2 and NO transport on aortic aneurysm development. To enable us to draw definitive conclusions, it is imperative that we expand our sample size to include a more substantial pool of healthy controls and patients, taking into account diverse locations of aortic aneurysms. Nonetheless, our study was primarily aimed at establishing a framework for modeling species transport and proposing a set of hemodynamic and biochemical biomarkers that could be evaluated in more significant population studies. Secondly, while numerous studies presented approaches for a multi-layer representation of (simple) arterial wall [40,41], we assumed a homogeneous single-layer aortic wall approximation. In reality, the aortic wall is composed of three layers (intima, media, and adventitia), each exhibiting unique physiological behavior. Therefore, our model lacks the capacity to determine the nature of mass transfer in each of the layers. However, we established the properties of the wall using scaled averages based on the respective properties of intima, media, and adventitia, thereby creating a model of the wall with overall average properties identical to a three-layer wall model. Thus, while we cannot provide insights into the specific behavior of each layer, we can reasonably capture the understanding of joined dynamics, especially for identifying hypoxia. Thirdly, we assumed a plug velocity profile at the inlet instead of a realistic one. However, our prior research has shown that if the root of the aorta is segmented correctly (as in our studied domains), the differences between the plug velocity profile and actual velocity profile are minimal [42]. Finally, the most significant limitation of our study is the absence of validation of O_2 and NO concentration within the aortic wall and lumen with direct measurements. The lack of validation originates from the current limitations of available methods for (in)direct non-invasive examination of these species in human arteries [9–12]. While an indirect comparison of our results can be made with invasive experiments that report on the concentration of O_2 using the hot cathode method on animal models [43,44], a direct comparison is not presently possible.

5. Summary and conclusions

This study aimed to simulate the mass transfer of O_2 and NO in the aorta of healthy control (HC) and patient (P) with root thoracic aortic aneurysm (TAA). To achieve this, a complex model was developed for the mass transfer of both species, incorporating hemoglobin-based transfer of O_2 in the domain, production of NO based on the local variation of WSS, and mass transfer (via diffusion) and consumption of both species in the arterial wall. The arterial wall was constructed with a single-layer assumption with homogeneous physical properties based on the average behavior of intima, media, and adventitia. Both simulations (HC and P) were based on 4D-flow MRI, with geometry and boundary conditions at the inlet and outlet directly based on the measurements. The simulated velocity field and WSS were validated against measured data, demonstrating good agreement.

The study revealed significant differences in hemodynamics between P and HC in and around the root, where P developed TAA. In these regions, WSS was markedly lower, while OSI and ECAP were elevated for P, whereas HC showed a more uniform distribution of these parameters. The distribution of O_2 and NO varied spatially in both the lumen and aortic wall, with apparent differences between healthy tissue and TAA in NO concentrations. In contrast, the concentration of O_2 was not influenced by the presence of TAA. However, the study demonstrated how aberrant blood flow could lead to hypoxia, indicating that O_2 should be monitored as a potential precursor for TAA pathogenesis.

In conclusion, the findings suggest that the studied quantities could be used as hemodynamical and biochemical predictors for TAA pathogenesis. However, due to the limited number of cases investigated, no statistically significant conclusions can be drawn. The authors propose that these hemodynamical and biochemical indicators be investigated in extensive population studies with multiple HC and patients with TAA, including longitudinal data. Such research could enhance the understanding of the aortic lumen and wall processes and ultimately improve the diagnosis and treatment of TAA.

Declaration of competing interest

The authors declare that they have no known competing financial interests or personal relationships that could have appeared to influence the work reported in this paper.

Funding

This research was financially supported by a grant from the Dutch Heart Foundation, The Netherlands (Grant Number CVON2018-08-RADAR).

Data availability

The data supporting this article have been uploaded to the data repository Dryad (https://doi.org/10.5061/dryad.2rbnzs7sq).

Appendix. Mesh dependency

Our mesh dependency analysis focused on two aspects:

1. Lumen-only - dependency of the simulated results on the varying size of volume mesh for lumen-only geometry
2. Lumen-wall - dependency of the simulated results on the varying number of extruded layers close to the lumen-wall interface for simulations with wall included

In this section, we will elaborate on these mesh dependency studies. As part of the analysis, we have calculated the Grid Convergence Index (GCI) to quantify findings, as presented in Table A.6 for both cases.

Lumen-only

To perform the mesh dependency study, we have created three meshes: coarse (≈1 mil. polyhedral elements), medium (≈2 mil. polyhedral elements), and fine (≈4 mil polyhedral elements). After performing simulations, we compared WSS, as shown in Fig. A.11 at the surface (with detail on ascending aorta), and its local variation alongside an extracted line, as shown in Fig. A.12. We can see that the three meshes agree well upon qualitative analysis, with only a small variation.

Table A.6
Grid convergence index (GCI) estimation for the healthy control; f_1 is wall shear stress for the fine mesh, f_2 is for the medium mesh, and f_3 is for the coarse mesh; r is the remeshing factor, p is the order of convergence, $f_{h=0}$ is the Richardson solution, $GCI_{1,2}$ is the GCI for fine and medium mesh, and $GCI_{2,3}$ is the GCI for medium and coarse mesh.

		Lumen-only	Lumen-wall
WSS_3	[Pa]	4.51	4.40
WSS_2	[Pa]	4.76	3.92
WSS_1	[Pa]	4.85	3.88
r		2.00	2.25
p		1.42	3.29
$f_{h=0}$	[Pa]	4.90	3.88
$GCI_{1,2}$	[%]	1.43	0.08
$GCI_{2,3}$	[%]	3.90	1.144
Asymptotic?		1.019	0.992

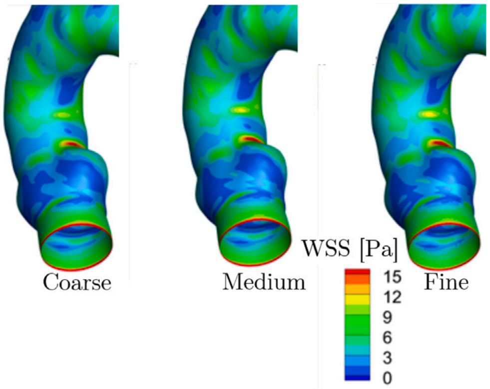

Fig. A.11. Wall shear stress (WSS [Pa]) for the healthy control with lumen-only approximation, using a coarse, medium, and fine mesh.

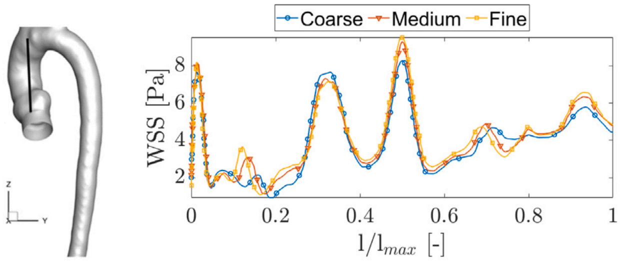

(a) (b)

Fig. A.12. Extracted local Wall shear stress (WSS [Pa]) alongside the line visualized in (a) with normalized length l/l_{max} [−] where l_{max} is the total distance of the line, for the healthy control with lumen-only approximation, using coarse, medium, and fine mesh.

Lumen-wall

We have adopted a different approach to the mesh sensitivity analysis for the case when the wall is included in the simulations. Here, we created three meshes with volume settings based on the medium mesh from the lumen-only analysis. The differences between the meshes were the number of extruded layers (the wall side) in the proximity of the lumen-wall interface, with two, five, and ten layers for the coarse, medium, and fine mesh, respectively. We performed blood flow simulations to test the meshes and calculated WSS on the lumen-wall interface. Subsequently (for visualization and analysis purposes), WSS was interpolated on the vasa vasorum, where we have performed the mesh sensitivity analysis, as shown in Fig. A.13 for the surface with detail on the ascending aorta and in Fig. A.14 for the local variation in WSS alongside an extracted line.

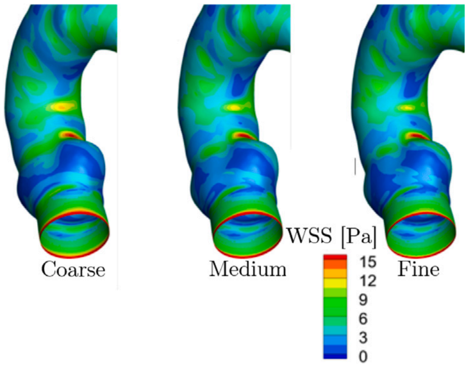

Fig. A.13. Wall shear stress (WSS [Pa]) for the healthy control with lumen-wall approximation, using a coarse, medium, and fine mesh.

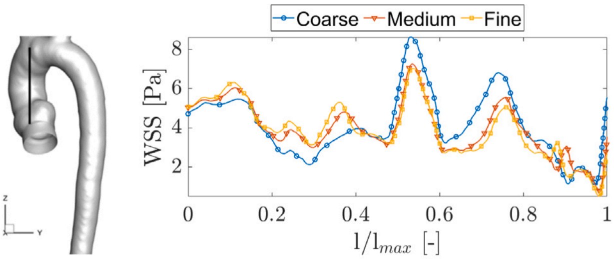

(a) (b)

Fig. A.14. Extracted local Wall shear stress (WSS [Pa]) alongside the line visualized in (a) with normalized length l/l_{max} [−] where l_{max} is the total distance of the line, for the healthy control with lumen-wall approximation, using coarse, medium, and fine mesh.

References

[1] 2014 ESC Guidelines on the diagnosis and treatment of aortic diseases, Eur. Heart J. 35 (41) (2014) 2873–2926, http://dx.doi.org/10.1093/eurheartj/ehu281.

[2] P. Visser, G.J.M. Akkersdijk, J.D. Blankensteijn, In-hospital operative mortality of ruptured abdominal aortic aneurysm: A population-based analysis of 5593 patients in The Netherlands over a 10-year period, Eur. J. Vasc. Endovasc. Surg. 30 (4) (2005) 359–364, http://dx.doi.org/10.1016/j.ejvs.2005.05.005.

[3] M. Billaud, J.C. Hill, T.D. Richards, T.G. Gleason, J.A. Phillippi, Medial hypoxia and adventitial vasa vasorum remodeling in human ascending aortic aneurysm, Front. Cardiovasc. Med. 5 (2018) http://dx.doi.org/10.3389/fcvm.2018.00124.

[4] H. Tanaka, N. Zaima, T. Sasaki, T. Hayasaka, N. Goto-Inoue, K. Onoue, K. Ikegami, Y. Morita, N. Yamamoto, Y. Mano, M. Sano, T. Saito, K. Sato, H. Konno, M. Setou, N. Unno, Adventitial vasa vasorum arteriosclerosis in abdominal aortic aneurysm, PLoS ONE 8 (2) (2013) 1–8, http://dx.doi.org/10.1371/journal.pone.0057398.

[5] M. Sano, N. Unno, T. Sasaki, S. Baba, R. Sugisawa, H. Tanaka, K. Inuzuka, N. Yamamoto, K. Sato, H. Konno, Topologic distributions of vasa vasorum and lymphatic vasa vasorum in the aortic adventitia – implications for the prevalence of aortic diseases, Atherosclerosis 247 (2016) 127–134, http://dx.doi.org/10.1016/j.atherosclerosis.2016.02.007.

[6] H. Wolinsky, S. Glagov, Nature of species differences in the medial distribution of aortic vasa vasorum in mammals, Circ. Res. 20 (4) (1967) 409–421, http://dx.doi.org/10.1161/01.RES.20.4.409.

[7] J. Oller, N. Méndez-Barbero, E.J. Ruiz, S. Villahoz, M. Renard, L.I. Canelas, A.M. Briones, R. Alberca, N. Lozano-Vidal, M.A. Hurlé, D. Milewicz, A. Evangelista, M. Salaices, J.F. Nistal, L.J. Jiménez-Borreguero, J. De Backer, M.R. Campanero, J.M. Redondo, Nitric oxide mediates aortic disease in mice deficient in the metalloprotease Adamts1 and in a mouse model of marfan syndrome, Nat. Med. 23 (2) (2017) 200–212, http://dx.doi.org/10.1038/nm.4266.

[8] A. de la Fuente-Alonso, M. Toral, A. Alfayate, M.J. Ruiz-Rodríguez, E. Bonzón-Kulichenko, G. Teixido-Tura, S. Martínez-Martínez, M.J. Méndez-Olivares, D. López-Maderuelo, I. González-Valdés, E. Garcia-Izquierdo, S. Mingo, C.E. Martín, L. Muiño-Mosquera, J. De Backer, J.F. Nistal, A. Forteza, A. Evangelista, J. Vázquez, M.R. Campanero, J.M. Redondo, Aortic disease in marfan syndrome is caused by overactivation of sGC-PRKG signaling by NO, Nature Commun. 12 (1) (2021) 2628, http://dx.doi.org/10.1038/s41467-021-22933-3.

[9] D.P. Guensch, M.C. Michel, S.P. Huettenmoser, B. Jung, P. Gulac, A. Segiser, S.L. Longnus, K. Fischer, The blood oxygen level dependent (BOLD) effect of in-vitro myoglobin and hemoglobin, Sci. Rep. 11 (1) (2021) 11464, http://dx.doi.org/10.1038/s41598-021-90908-x.

[10] J. Ruiz-Cabello, B. Barnett, P. Bottomley, J. Bulte, Fluorine (19f) MRS and MRI in biomedicine, NMR Biomed. 24 (2011) 114–129, http://dx.doi.org/10.1002/nbm.1570.

[11] A.H. Schmieder, S.D. Caruthers, J. Keupp, S.A. Wickline, G.M. Lanza, Recent advances in 19fluorine magnetic resonance imaging with perfluorocarbon emulsions, Engineering 1 (4) (2015) 475–489, http://dx.doi.org/10.15302/J-ENG-2015103.

[12] S. Chaudhary, N. Akter, A. Rajeev, M. Hwang, S. Sirsi, Hemoglobin microbubbles for in vivo blood oxygen level dependent imaging: Boldly moving beyond MRI, J. Acoust. Soc. Am. 150 (4) (2021) A27, http://dx.doi.org/10.1121/10.0007507.

[13] R. Perinajová, J.F. Juffermans, J.J. Westenberg, R.L. van der Palen, P.J. van den Boogaard, H.J. Lamb, S. Kenjereš, Geometrically induced wall shear stress variability in CFD-mri coupled simulations of blood flow in the thoracic aortas, Comput. Biol. Med. 133 (2021) 104385, http://dx.doi.org/10.1016/j.compbiomed.2021.104385.

[14] R. Perinajová, J.F. Juffermans, J.L. Mercado, J.-P. Aben, L. Ledoux, J.J.M. Westenberg, H.J. Lamb, S. Kenjereš, Assessment of turbulent blood flow and wall shear stress in aortic coarctation using image-based simulations, BioMed. Eng. OnLine 20 (1) (2021) 84, http://dx.doi.org/10.1186/s12938-021-00921-4.

[15] J. Moore, C.R. Ethier, Oxygen mass transfer calculations in large arteries, J. Biomech. Eng. 119 (4) (1997) 469–475, http://dx.doi.org/10.1115/1.2798295.

[16] C. Cheng, R. van Haperen, M. de Waard, L.C.A. van Damme, D. Tempel, L. Hanemaaijer, G.W.A. van Cappellen, J. Bos, C.J. Slager, D.J. Duncker, A.F.W. van der Steen, R. de Crom, R. Krams, Shear stress affects the intracellular distribution of eNOS: direct demonstration by a novel in vivo technique, Blood 106 (12) (2005) 3691–3698, http://dx.doi.org/10.1182/blood-2005-06-2326.

[17] C. Cheng, D. Tempel, A. Oostlander, F. Helderman, F. Gijsen, J. Wentzel, R. van Haperen, D.B. Haitsma, P.W. Serruys, A.F. van der Steen, R. de Crom, R. Krams, Rapamycin modulates the eNOS vs. shear stress relationship, Cardiovasc. Res. 78 (1) (2007) 123–129, http://dx.doi.org/10.1093/cvr/cvm103.

[18] S. Tada, J.M. Tarbell, Oxygen mass transport in a compliant carotid bifurcation model, Ann. Biomed. Eng. 34 (9) (2006) 1389–1399, http://dx.doi.org/10.1007/s10439-006-9155-z.

[19] A.M. Plata, S.J. Sherwin, R. Krams, Endothelial nitric oxide production and transport in flow chambers: The importance of convection, Ann. Biomed. Eng. 38 (9) (2010) 2805–2816, http://dx.doi.org/10.1007/s10439-010-0039-x.

[20] X. Chen, D.G. Buerk, K.A. Barbee, P. Kirby, D. Jaron, 3D network model of NO transport in tissue, Med. Biol. Eng. Comput. 49 (6) (2011) 633, http://dx.doi.org/10.1007/s11517-011-0758-7.

[21] X. Liu, Z. Wang, P. Zhao, Z. Fan, A. Sun, F. Zhan, Y. Fan, X. Deng, Nitric oxide transport in normal human thoracic aorta: Effects of hemodynamics and nitric oxide scavengers, PLoS ONE 9 (2014) 1–10, http://dx.doi.org/10.1371/journal.pone.0112395.

[22] X. Li, X. Liu, P. Zhang, C. Feng, A. Sun, H. Kang, X. Deng, Y. Fan, Numerical simulation of haemodynamics and low-density lipoprotein transport in the rabbit aorta and their correlation with atherosclerotic plaque thickness, J. R. Soc. Interface 14 (129) (2017) 20170140, http://dx.doi.org/10.1098/rsif.2017.0140.

[23] S. Qian, T. Ma, N. Zhang, X. Liu, P. Zhao, X. Li, D. Chen, L. Hu, L. Chang, L. Xu, X. Deng, Y. Fan, Spatiotemporal transfer of nitric oxide in patient-specific atherosclerotic carotid artery bifurcations with MRI and computational fluid dynamics modeling, Comput. Biol. Med. 125 (2020) 104015, http://dx.doi.org/10.1016/j.compbiomed.2020.104015.

[24] B.W. Allen, J.S. Stamler, C.A. Piantadosi, Hemoglobin, nitric oxide and molecular mechanisms of hypoxic vasodilation, Trends Mol. Med. 15 (10) (2009) 452–460, http://dx.doi.org/10.1016/j.molmed.2009.08.002.

[25] M. Bukač, M. Alber, Multi-component model of intramural hematoma, J. Biomech. 50 (2017) 42–49, http://dx.doi.org/10.1016/j.jbiomech.2016.11.040.

[26] L. Ai, K. Vafai, A coupling model for macromolecule transport in a stenosed arterial wall, Int. J. Heat Mass Transfer 49 (2006) 1568–1591, http://dx.doi.org/10.1016/j.ijheatmasstransfer.2005.10.041.

[27] R. Perinajová, P. van Ooij, S. Kenjereš, On the identification of hypoxic regions in subject-specific cerebral vasculature by combined CFD/mri, R. Soc. Open Sci. 10 (1) (2023) 220645, http://dx.doi.org/10.1098/rsos.220645.

[28] S. Chung, K. Vafai, Effect of the fluid–structure interactions on low-density lipoprotein transportwithin a multi-layered arterial wall, J. Biomech. 45 (2) (2012) 371–381, http://dx.doi.org/10.1016/j.jbiomech.2011.10.002.

[29] G. Pontrelli, F. de Monte, A multi-layer porous wall model for coronary drug-eluting stents, Int. J. Heat Mass Transfer 53 (19) (2010) 3629–3637, http://dx.doi.org/10.1016/j.ijheatmasstransfer.2010.03.031.

[30] G. Pontrelli, A. Di Mascio, F. de Monte, Local mass non-equilibrium dynamics in multi-layered porous media: application to the drug-eluting stent, Int. J. Heat Mass Transfer 66 (2013) 844–854, http://dx.doi.org/10.1016/j.ijheatmasstransfer.2013.07.041.

[31] F. Gijsen, F. van de Vosse, J. Janssen, The influence of the non-Newtonian properties of blood on the flow in large arteries: steady flow in a carotid bifurcation model, J. Biomech. 32 (6) (1999) 601–608, http://dx.doi.org/10.1016/S0021-9290(99)00015-9.

[32] E. Ortiz-Prado, J. Dunn, J. Vasconez, D. Castillo, G. Viscor, Partial pressure of oxygen in the human body: a general review., Am. J. Blood Res. 9 (1) (2019) 1–14.

[33] M.Y. Salmasi, S. Pirola, S. Sasidharan, S.M. Fisichella, A. Redaelli, O.A. Jarral, D.P. O'Regan, A.Y. Oo, J.E. Moore, X.Y. Xu, T. Athanasiou, High wall shear stress can predict wall degradation in ascending aortic aneurysms: An integrated biomechanics study, Front. Bioeng. Biotech. 9 (2021) http://dx.doi.org/10.3389/fbioe.2021.750656.

[34] A.J. Boyd, D.C. Kuhn, R.J. Lozowy, G.P. Kulbisky, Low wall shear stress predominates at sites of abdominal aortic aneurysm rupture, J. Vasc. Surg. 63 (6) (2016) 1613–1619, http://dx.doi.org/10.1016/j.jvs.2015.01.040.

[35] Y.-S.J. Li, J.H. Haga, S. Chien, Molecular basis of the effects of shear stress on vascular endothelial cells, J. Biomech. 38 (10) (2005) 1949–1971, http://dx.doi.org/10.1016/j.jbiomech.2004.09.030.

[36] D.A. Chistiakov, A.N. Orekhov, Y.V. Bobryshev, Effects of shear stress on endothelial cells: go with the flow, Acta Physiol. 219 (2) (2017) 382–408, doi: https://doi-org.tudelft.idm.oclc.org/10.1111/apha.12725.

[37] L. Peng, Y. Qiu, Z. Yang, D. Yuan, C. Dai, D. Li, Y. Jiang, T. Zheng, Patient-specific computational hemodynamic analysis for interrupted aortic arch in an adult: Implications for aortic dissection initiation, Sci. Rep. 9 (1) (2019) 8600, http://dx.doi.org/10.1038/s41598-019-45097-z.

[38] E.P. Manning, A.B. Ramachandra, J.C. Schupp, C. Cavinato, M.S.B. Raredon, T. Bärnthaler, C. Cosme, I. Singh, G. Tellides, N. Kaminski, J.D. Humphrey, Mechanisms of hypoxia-induced pulmonary arterial stiffening in mice revealed by a functional genetics assay of structural, functional, and transcriptomic data, Front. Physiol. 12 (2021) http://dx.doi.org/10.3389/fphys.2021.726253.

[39] O.J. Erdozain, S. Pegrum, V.R. Winrow, M. Horrocks, C.R. Stevens, Hypoxia in abdominal aortic aneurysm supports a role for HIF-1α and ets-1 as drivers of matrix metalloproteinase upregulation in human aortic smooth muscle cells, J. Vasc. Res. 48 (2) (2011) 163–170, http://dx.doi.org/10.1159/000318806.

[40] S. Kenjereš, A. de Loor, Modelling and simulation of low-density lipoprotein transport through multi-layered wall of an anatomically realistic carotid artery bifurcation, J. R. Soc. Interface 11 (91) (2014) 20130941, http://dx.doi.org/10.1098/rsif.2013.0941.

[41] S. Kenjereš, J. van der Krieke, C. Li, Endothelium resolving simulations of wall shear-stress dependent mass transfer of LDL in diseased coronary arteries, Comput. Biol. Med. 114 (2019) 103453, http://dx.doi.org/10.1016/j.compbiomed.2019.103453.

[42] R. Perinajova, T. van de Ven, E. Roelse, F. Xu, J. Juffermans, J. Westenberg, H.J. Lamb, S. Kenjereš, A comprehensive MRI-based computational model of blood flow in compliant aorta using radial basis function interpolation, SSRN Electr. J. (2022) http://dx.doi.org/10.2139/ssrn.4029428.

[43] D.G. Buerk, T.K. Goldstick, Arterial wall oxygen consumption rate varies spatially, Am. J. Physiol.-Heart Circ. Physiol. 243 (6) (1982) H948–H958, http://dx.doi.org/10.1152/ajpheart.1982.243.6.H948, PMID: 7149047.

[44] S.M. Santilli, R.B. Stevens, J.G. Anderson, W.D. Payne, M.D. Caldwell, Transarterial wall oxygen gradients at the dog carotid bifurcation, Am. J. Physiol.-Heart Circ. Physiol. 268 (1) (1995) H155–H161, http://dx.doi.org/10.1152/ajpheart.1995.268.1.H155, PMID: 7840259.